Volume 1 | Number 1 | Jan 2013 | Pages 1–100

Catalysis
Science &
Technology

www.rsc.org/catalysis

ROYAL SOCIETY
OF CHEMISTRY

This is an *Accepted Manuscript*, which has been through the Royal Society of Chemistry peer review process and has been accepted for publication.

Accepted Manuscripts are published online shortly after acceptance, before technical editing, formatting and proof reading. Using this free service, authors can make their results available to the community, in citable form, before we publish the edited article. We will replace this *Accepted Manuscript* with the edited and formatted *Advance Article* as soon as it is available.

You can find more information about *Accepted Manuscripts* in the **Information for Authors**.

Please note that technical editing may introduce minor changes to the text and/or graphics, which may alter content. The journal's standard **Terms & Conditions** and the **Ethical guidelines** still apply. In no event shall the Royal Society of Chemistry be held responsible for any errors or omissions in this *Accepted Manuscript* or any consequences arising from the use of any information it contains.

Catalysis Science & Technology

ARTICLE

Hägg Carbide Surfaces Induced Pt Morphological Changes: A Theoretical Insight†

Yurong He,[a,b,c] Peng Zhao,[a,b,c] Wenping Guo,[b] Yong Yang,[a,b] Chun-Fang Huo,*[b] Yong-Wang Li,*[a,b] and Xiao-Dong Wen*[a,b]

A comprehensive spin-polarized density functional theory (DFT) combining with ab initio molecular dynamic (AIMD) simulation have been performed to explore the structures, energies, and diffusion behavior of platinum on Fe_5C_2 surfaces with importance in Fischer-Tropsch (F-T) catalysis. The results indicate that the morphology of Pt promoter on Hägg carbide highly depends on the surface structure of Fe_5C_2. The $Fe_5C_2(111)$ surface shows stronger Pt affinity than the $Fe_5C_2(100)$ surface, while the $Fe_5C_2(100)$ surface has stronger Pt_n aggregation ability. Under the realistic iron-based F-T reaction conditions, the adsorbed Pt atoms can diffuse easily, and tend to aggregate following the line-band-layer mode on $Fe_5C_2(100)$. While on the $Fe_5C_2(111)$ surface, the adsorbed Pt atoms prefer to sitting in the most stable sites, and form the dispersed structures rather than the aggregated structures until the coverage of Pt is above 2/7 (the surface atom ratio of Pt to Fe). In addition, the three-dimensional structures are not favored on both surfaces because of the stronger Fe-Pt interaction over the Pt-Pt bonding. The adsorbed Pt atoms are with negative charges, and the stronger electron transfer is observed on the $Fe_5C_2(100)$ surface, especially at the low coverage.

1. Introduction

Under the background of oil resources depletion, the Fischer-Tropsch synthesis (FTS),[1,2] which allows to convert synthesis gas (CO+H_2) into clean transportation fuels and valuable chemicals with catalysts based on transition metals such as iron, cobalt, and ruthenium, is gaining increasing importance. As syngas can be produced by steam reforming and/or partial oxidation of coal, nature gas, biomass, FTS becomes a potential alternative to crude oil.

The iron-based catalysts were widely used in industrial FTS because of their low cost, high activity, and high water gas shift (WGS) reaction activity, which is helpful to convert coal-derived syngas with a low H_2/CO ratio.[3,4] The catalyst precursor (α-Fe_2O_3) has to be reduced before the catalyst becomes active and the reduced phases are inevitably carburized to carbide under FTS conditions.[5] Diverse carbide phases have been identified under FTS conditions, such as ε'-$Fe_{2.2}C$, ε-Fe_2C, χ-Fe_5C_2, θ-Fe_3C, and Fe_7C_3.[5-8] Among these, χ-

Fe_5C_2 (Hägg) has been experimentally found to be one of the most important active iron carbide phases experimentally.[8-11]

For the industrial Fe-based catalysts, promoters are necessary to obtain the good performance. Adding potassium favors CO dissociative adsorption,[12-14] leading to the higher FTS activity, selectivity to olefins, and higher molecular weight products.[15,16] SiO_2 and Al_2O_3 are usually used as structural promoters and supports to enhance the mechanical stability of the catalysts and stabilize high-surface area iron phases against sintering.[17,18] Copper is generally regarded as a reduction promoter facilitating the reduction of catalyst precursor.[19,20]

Platinum, also known as group VIII noble metal, was extensively studied as a promoter of cobalt-based Fischer–Tropsch catalysts since it could facilitate the reduction of cobalt at lower temperature by the hydrogen spillover from the noble metal particles to cobalt.[21-24] As a promoter for iron-based catalysts, platinum also affects the catalytic performance remarkably although few studies were reported. Xu et al.[25] prepared silica-supported iron catalysts using acetone evaporative deposition technique and found that the addition of Pt improves the reducibility of iron and increases the activity of FTS as well as WGS reaction. Further research by them demonstrated that Pt addition induces an increase in the fractions of highly dispersed Fe_3O_4 and Fe_5C_2 during the pretreatments of catalysts.[26] Similarly, Yu et al.[27] found that impregnating Pt facilitates the reduction and carburization of Fe_2O_3, increases the FTS activity, and suppresses the selectivity of light hydrocarbons and olefins. Moreover, Kovalchuk et al.[28] found the effects of Pt additive on the catalytic properties of silica-supported Fe catalysts in CO hydrogenation are similar to

a. State Key Laboratory of Coal Conversion, Institute of Coal Chemistry, Chinese Academy of Sciences, Taiyuan, 030001, China;
b. National Energy Center for Coal to Liquids, Synfuels China Co., Ltd, Huairou District, Beijing, 101400, China;
c. University of Chinese Academy of Sciences, No.19A Yuquan Road, Beijing, 100049, China.

* To whom correspondence should be addressed: huochun-fang@synfuelschina.com.cn; ywl@sxicc.ac.cn and wxd@sxicc.ac.cn

those of potassium, which shifts the product distribution to higher molecular weight (C_{4+}) olefins. Other noble metals, Pd, Ru, and Rh, also facilitate the reduction and carburization, and enhance the FTS activity.[29-34] For the product distribution, Luo et al.[29] and Minnermann et al.[30] reported that Pd promoter shifts the selectivity to longer chain hydrocarbons and significantly decreases the ratio of olefin to paraffin due to its hydrogenation property, which is similar to Pt. While Li et al.[33] and Wang et al.[34] found that Ru promoter hinders C_{5+} formation and increases the CH_4 selectivity.

It is noted that as illustrated by Mössbauer isomer shift, in the supported PtFe catalysts, electrons transfer from iron to platinum leading to a decrease in the electron density on iron, which is considered to be the opposite effect with alkali.[35] Why the noble metals Pt and Pd promoted catalysts have the similar catalytic performances to potassium? The studies on the interaction between noble metals and iron catalysts are still highly desired to rational design highly efficient FTS catalysts.

Note that the catalytic properties are obviously influenced by the specific geometrical and electronic features of the supported metal clusters, as reviewed by Viñes et. al.[36-38] However, experimentally, it is difficult to observe the patterns of promoter metals on the iron catalysts, especially on the active phases of the catalysts, due to the facile phase change of the carbides as well as the low content and high dispersion of the promoters. Qiu et al. synthesized a high performance catalyst for methanol electro-oxidation with the Pt nanoparticles around 6nm well dispersed on the NbC nanowires.[39] Yu et al.[27] showed that the impregnated Pt with crystallite diameter about 2 nm is well dispersed on the iron catalysts at a very high surface Pt/Fe weight ratio of 46.4/100. In addition, mono-dispersed Pt atoms are reported as single atom catalysts on the surfaces of iron oxide nanocrystallites[40] and θ-alumina (Al_2O_3).[41] The detailed structural information of Pt/Fe interface and the interaction between Pt and iron carbide are scarce, although they are the basis for understanding of the Pt promotion mechanisms.

Herein, we intend to theoretically investigate the effects of the noble metal platinum on Fe_5C_2 to obtain the structural, electronic properties of the Pt/Fe_5C_2. First, we systematically calculate/predict the Pt_n adsorption structures and energies on the $Fe_5C_2(100)$ and $Fe_5C_2(111)$ surfaces utilizing density functional theory (DFT). Subsequently, the diffusion of single Pt atom on each surface is analyzed to show the kinetic possibility to form the most stable structure of Pt_n on the Fe_5C_2 surfaces. Furthermore, ab initio molecular dynamic (AIMD) studies are carried out to validate the structures optimized by DFT calculation under the realistic reaction conditions of the Fe-based FTS. The purpose of the work is to provide a theoretical insight on the interaction between Pt and Fe_5C_2.

2. Computational details

2.1. Methods

All adsorption calculations were carried out at the density functional theory (DFT) level by using the Vienna Ab intio

Simulation Package (Vasp).[42,43] Given the good performance on describing transition metals and carbides,[44,45] the electron exchange and correlation energy was treated within the Perdew-Burke-Ernzerhof (PBE) functional [46] of generalized gradient approximations (GGA).[47] The election-ion interaction was described by the projector augmented wave (PAW)[48,49] method, and the iterative solutions of Kohn-Sham equations was done using a plane-wave basis set with a cutoff energy of 400 eV. The sampling of the Brillouin zone was performed using a Monkhorst-Pack scheme. Spin-polarization was included to calculate the adsorption energy accurately in the magnetic systems of χ-Fe_5C_2. Electron smearing was employed via a 2nd-order Methfessel-Paxton scheme and the width of the smearing was set as σ=0.2 eV to ensure accurate energy with errors less than 1 meV per atom. The convergence criteria for electronic self-consistent interactions and all forces were set to 10^{-4} eV and 0.03 eV/Å, respectively. For evaluating the Pt diffusion barriers, all transition states and pathways were obtained using the climbing image nudged elastic band (CINEB) method[50-52] and vibrational frequencies were analyzed to evaluate a transition state with only one imaginary frequency.

Ab initio molecular dynamics (AIMD) calculations were performed using a CP2K package[53,54] with PBE functional. The wave functions were expanded in a molecularly optimized double-ζ Gaussian basis set to minimize basis set superposition errors.[55] An additional auxiliary plane wave[56] basis of 350 Ry energy cutoff was used for the calculation of the electrostatic energy terms. Exchange and correlation core electrons were modeled by scalar relativistic norm-conserving pseudopotentials[57,58] with 4, 16, and 10 valence electrons of C, Fe, and Pt, respectively. All molecular dynamics simulations are performed by sampling the canonical (NVT) ensemble employing Nose–Hoover thermostats[59,60] with a time step of 1 fs during 20 ps of well-equilibrated trajectory. The relatively short time scales of AIMD limit sampling to only very fast, low-energy barrier events and preclude the observation slow processes. To partially overcome this limitation, we have performed simulations at a relatively high temperature of 1000K to more rapidly explore a large volume of phase space.

For Pt_n clusters in gas phase, Gaussian smearing method with a width 0.001 eV was used to determine the partial occupancies and the calculations are performed at a single Gamma point. According to the work by Tian et al.,[61] the average aggregation energy [$E_{agg}(Pt_{gas})$] can be defined as in equation 1 and the growth energy [$E_{growth}(Pt_{gas})$] is calculated using equation 2.

$$E_{agg}(Pt_{gas}) = [E(Pt_{n/gas}) - nE(Pt_{gas})]/n \qquad \text{Eq. 1}$$

$$E_{growth}(Pt_{gas}) = E(Pt_{n/gas}) - E(Pt_{n-1/gas}) - E(Pt_{gas}) \qquad \text{Eq. 2}$$

Where $E(Pt_{n/gas})$ and $E(Pt_{gas})$ are the total energy of the cluster of n platinum atoms and of a isolated platinum atom in gas phase, respectively. Actually, minus $E_{agg}(Pt_{gas})$ equates to the binding energy per atom mentioned in literature.[62] The growth energy can help us to understand the formation reaction of $Pt_{n-1} + Pt_1 \rightarrow Pt_n$, and the more negative the growth energy, the easier the Pt_n formation.

For Pt_n adsorption on the surface, the total adsorption energy $[E(Pt_{n/ads})]$ is defined by equation 3 and the average adsorption energy $[E(Pt_{ads/av})]$ is defined in equation 4, where $E(Pt)_n/slab$ is the total energy of the Pt_n adsorbed system, $E(slab)$ is the total energy of the clean surface and n is the number of the adsorbed Pt atoms.

$$E(Pt_{n/ads}) = E(Pt)_n/slab - E(slab) - nE(Pt_{gas}) \quad \text{Eq. 3}$$

$$E(Pt_{ads/av}) = E(Pt_{n/ads})/n \quad \text{Eq. 4}$$

In addition, like in gas phase, we also define the average aggregation energy $[E_{agg}(Pt_{ads})]$ of adsorbed Pt_n on the surfaces according to equation 5; and the more negative the aggregation energy of surface Pt_n, the more stable of Pt_n on the surfaces. It should be noted that surface Pt_n in this study including both Pt_n clusters and n-dispersed Pt atoms on surfaces.

$$E_{agg}(Pt_{ads}) = [E(Pt_{n/ads}) - nE(Pt_{ads})]/n \quad \text{Eq. 5}$$

Furthermore, we also define the growth energy according to equation 6. On one hand, the more negative the growth energy $[E_{growth}(Pt_{ads})]$ of the Pt_n adsorbed on the surfaces, the stronger the ability of Pt_{n-1} to get one Pt atom from the surface to form the Pt_n. On the other hand, if the $[E_{growth}(Pt_{ads})]$ is positive, the dispersed structure is thermodynamically more stable.
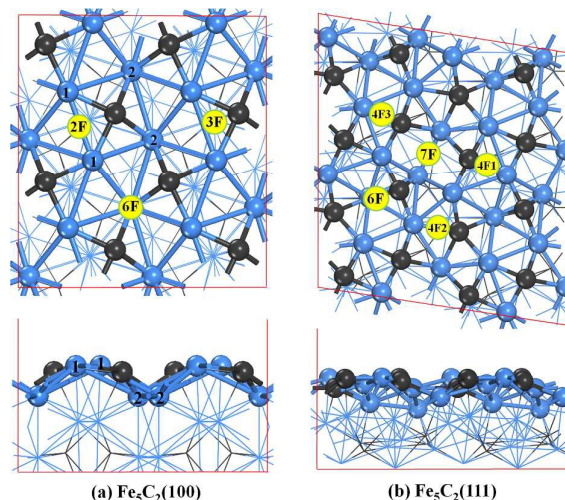
$$E_{growth}(Pt_{ads}) = E(Pt_{n/ads}) - E(Pt_{n-1/ads}) - E(Pt_{ads}) \quad \text{Eq. 6}$$

2.2. Models

The Hägg iron carbide has a monoclinic unit cell (Fig. 1a). Using PAW-PBE method, the calculated crystallographic parameters (a = 11.545 Å, b = 4.496 Å, c = 4.982 Å, and β = 97.6°) and magnetic moment (1.73 μB) agree reasonably with the experimental data (a = 11.558 Å, b = 4.579 Å, c = 5.069 Å,
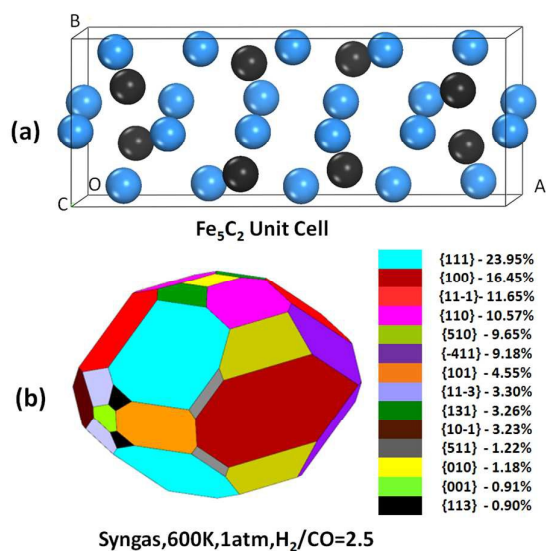
Fig. 2 Structures of the surfaces and adsorption sites for single Pt atom on the $Fe_5C_2(100)$ and $Fe_5C_2(111)$ surfaces; two-fold (2F), three-fold (3F), four-fold (4F1, 4F2, and 4F3), six-fold (6F), and seven-fold (7F) sites (blue balls for Fe atoms and black balls for the C atoms)

β= 97.8°; and 1.72 − 1.75 μB[63]). According to the previous research[64] (Fig. 1b), the exposed area ratios of $Fe_5C_2(100)$ and (111) surfaces in equilibrium shape based on Wulff construction under the practical FTS condition (600K, 1atm, syngas H_2/CO = 2.5) are larger than others, which is about 16.5% and 24.0% respectively. So, we choose these two facets with the most stable terminations (1.82 J/m² for $(100)_{0.402}$ surface and 2.01 J/m² for $(111)_{0.621}$ surface) as examples to investigate the structures of Pt_n on catalysts.
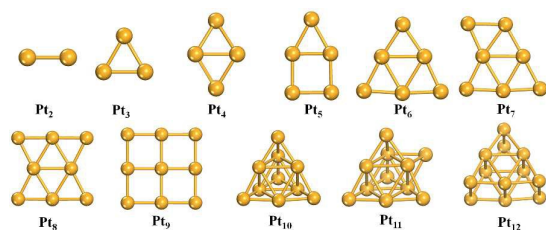
For exploring the adsorption structures and energies of Pt_n, the periodic slab modes were adopted. Both the $Fe_5C_2(100)$ and $Fe_5C_2(111)$ surfaces have exposed surface iron and carbon atoms. To model the $Fe_5C_2(100)$ and (111) surfaces (Fig. 2a and 2b), the $p(2\times2)$ supercells containing six iron layers and three carbon layers (6Fe+3C; 5.90 Å) as well as ten iron layers and four carbon layers (10Fe+4C; 4.72 Å) were used, respectively. In our calculations, the top 2Fe+1C layers of (100) and the top 4Fe+2C layers of (111) were relaxed, while the remaining bottom layers were fixed in their bulk positions. The sizes of the (100) and (111) surfaces are 9.0×10.0 and 12.4×13.4 Å², respectively. Without counting the adsorbates, the vacuum gap space between slabs was set to 15 Å to avoid significant slab interaction. According to the lattice sizes, 2×2×1 k-point grid sampling within the Brillouin zones was set. All Pt_n clusters in gas phase were calculated using a 15Å×15Å×15Å cubic unit cell with a 3×3×3 k-point grid.

3. Results

3.1. Free standing Pt_n Cluster

Though the ground state geometries of small Pt clusters have been reported by several researches in the past decade,[62,65-71] remarkable differences of the structures and

Fig. 1 The unit cell of Hägg iron carbide (a) and the equilibrium shape based on Wulff construction under the condition of 600K, 1atm and syngas H_2/CO = 2.5 (b).

Fig. 3 Most stable gas phase structures for Pt_n (n=1-12) clusters

energies exist depending on the different theoretical methods. Herein, we have investigated the low-lying isomers of gas phase Pt_n (n=2-12) clusters[62,65-70] with the PAW-PBE method and the most stable structures are shown in Fig 3. The average aggregation energies of the Pt_n isomers are given in **ESI†** (Table S1). The most stable Pt_3-Pt_9 clusters grow by forming two dimensional structures, which are in excellent agreement with the ground state structures computed by K. Bhattacharyya et al.[68] From Pt_{10} onwards, the most stable Pt_n clusters favor three-dimensional patterns. The tetrahedron structure, with the Pt atoms connected by triangular units, coincides with the most stable Pt_{10} cluster discovered before.[62,65,68] The most stable Pt_{11} cluster is formed by adding one Pt atom to the tetrahedral Pt_{10} at a three-fold coordination site. For Pt_{12}, the most stable cluster consists of two Pt_6 planar clusters, which is in agreement with the conclusion that it is easy to grow a platinum monolayer or multilayer in gas phase.[62] As listed in Table 1, the average Pt-Pt bond distances increase with the cluster size; and that of Pt_2 calculated with PBE functional is slightly shorter than other computational[62,65,68] and the experimental[72] values.

Table 1 also displays the negative average aggregated energies [-E_{agg}(Pt_{gas})] (i.e.; binding energies) and the growth energies [E_{growth}(Pt_{gas})] of Pt_n in gas phase. Our computed binding energy of Pt_2 is in the range of the experimental values derived from the mass spectrometry study of the gaseous diatomic metallic molecules,[72] but is higher than other theoretical results[62,68,69] except for that calculated with local spin density approximation (LSDA).[67] The binding energies generally increase with the increase of the cluster size, indicating that, in gas phase, the larger aggregated Pt_n cluster has the higher stability. The most negative E_{growth}(Pt_{gas}) of tetrahedral Pt_{10} suggests a relative stability of symmetric structure, which is in agreement with the conclusion from Bhattacharyya.[68]

3.2. Pt_n Adsorption on Fe_5C_2(100) Surface

As shown in Fig. 2a, in one p(2×2) supercell of Fe_5C_2(100), the sixteen exposed iron atoms link as four zigzag lines and distribute in two layers forming a stepped surface, and eight carbon atoms locate in the tilted 4-fold sites. Eight Fe#1 and eight Fe#2 atoms are equal, respectively.

For single Pt atom adsorption, all the possible sites, top, bridge, and three or more coordination sites, are considered in our initial configurations. After the optimization, three

Table 1 Average aggregation energy [E_{agg}(Pt_{gas}), eV] and growth energy [E_{growth}(Pt_{gas}), eV] as well as the average Pt-Pt distance (R, Å) of Pt_n clusters in gas phase

Pt_n	-E_{agg}(Pt_{gas})/eV	E_{growth}(Pt_{gas})/eV	R/Å
Pt_2	1.95	-3.90	2.32
	1.86[a]		2.33[a]
	1.63[b]		2.45[b]
	1.76[c]		2.34[c]
	1.86±0.10[d]		2.34[d]
	2.13[e]		2.33[e]
Pt_3	2.50	-3.58	2.48
	2.41[a]		2.49[a]
	2.22[b]		2.57[b]
	2.33[c]		2.47[c]
Pt_4	2.80	-3.70	2.51
	2.70[a]		2.51[a]
	2.62[c]		2.51~2.58[c]
Pt_5	3.06	-4.10	2.46
	2.96[a]		
	2.89[c]		2.43~2.51[c]
Pt_6	3.31	-4.56	2.54
	3.21[a]		
	2.94[b]		
	3.08[c]		2.49~2.61[c]
Pt_7	3.37	-3.73	2.53
	3.26[a]		
Pt_8	3.49	-4.36	2.52
	3.37[a]		
	3.11[b]		
	3.27[c]		2.47~2.67[c]
Pt_9	3.65	-4.94	2.45
	3.54[a]		
	3.12[b]		
	3.41[c]		2.44~2.46[c]
Pt_{10}	3.80	-5.12	2.65
	3.71[a]		
	3.64[c]		2.51~2.81[c]
Pt_{11}	3.80	-3.75	2.66
	3.86	-4.58	2.59
Pt_{12}	3.86	-4.58	2.59

(a) Calculated results (PAW, GGA method) from Ref 68. (b) Calculated results (effective core potential, PW91 method) from Ref 69. (c) Calculated results (Ultrasoft Pseudopotential, PW91) from Ref 62. (d) Experimental results from Ref 72. (e) Calculated results (ultrasoft pseudopotential, LSDA method) from Ref 67.

different sites are found on the Fe_5C_2(100) surface. The six-fold site (6F) locates on the top of the second layer Fe atom and consists of three Fe#1 and one Fe#2 as well as two C atoms. The three-fold (3F) consists of two Fe#1 and one C atoms, and the two-fold (2F) site consists of two Fe#1 atoms, respectively.

For Pt_n adsorption on the Fe_5C_2(100) surface, aggregated and dispersed adsorption modes have been examined. Our results for the adsorption of Pt_n (n = 1-12, 16) show that mono-layer two-dimensional (2D) adsorption configurations are more stable than three-dimensional (3D) clusters. Therefore we mainly discuss the most stable two-dimensional configurations while the energies and structures of three-dimensional configurations as well as the less stable configurations are given in **ESI†** (Fig. S2-5) for comparison. The results of the most stable Pt_n (n = 1-12, 16) adsorption on the Fe_5C_2(100) surface are listed in Table 2 and the corresponding adsorption configurations are shown in Fig. 4.

3.2.1. Pt_n adsorption.

As shown in Fig. 4, the most stable adsorption site for single Pt atom on Fe_5C_2 (100) is the 6F site, and the corresponding adsorption energy is -4.97 eV.

Based on **Pt₁** adsorption, we get the most stable configurations for Pt_2 in each adsorption mode. The aggregated mode (**Pt₂-a**) having two Pt atoms at the nearest neighbor 6F sites with the Pt-Pt distance of 2.78 Å is more stable, and the adsorption energy is -10.16 eV, while the dispersed mode (**Pt₂-d**) with two Pt atoms located at the isolated 6F sites is less stable (-9.90 eV).

On the basis of **Pt₂-a** and **Pt₂-d**, the most stable linear (**Pt₃-a**) and dispersed (**Pt₃-d**) adsorption configurations are obtained, in which all Pt atoms at the 6F sites. The aggregated linear Pt_3 adsorption configuration (**Pt₃-a**) has the average Pt-Pt distance of 2.76 Å, and is more stable than the dispersed configuration (**Pt₃-d**) by 0.65 eV.

For n = 4, the most stable structure is also the linear mode (**Pt₄-a**, -21.29 eV) by adding one Pt atom at the 6F site to **Pt₃-a**. After optimization, the four Pt atoms shift to 4-fold sites consisted by two Fe#1, one Fe#2, and one C atoms, and the average Pt-Pt distance shortens to 2.72 Å. This linear **Pt₄-a** structure properly fits the zigzag groove between two ridged Fe#1 lines. While the dispersed mode (**Pt₄-d**) has a little lower average adsorption energy than **Pt₁** (-4.91 vs. −4.97 eV), indicating a mild lateral repulsive interaction. It is also should be noted that the linear-based growth mode has negative growth energies, and the longer the chain the more negative the growth energy, while positive growth energies are found for the dispersed mode (Table 2). That is to say, at very low coverage, Pt prefers to grow in linear mode, and the dispersed mode is unfavorable on Fe_5C_2 (100) surface.

Based on the above results, for subsequent Pt_n (n>4) adsorption, only aggregated modes are taken into account. As displayed in Fig. 4, further addition of Pt atoms to **Pt₄-a** leads to form another Pt chain (aggregated mode a) or branched

structure (aggregated mode b), and gradually aggregate to monolayer Pt(111) structure. For the double-chain configurations, **Pt₅-a**, **Pt₆-a**, **Pt₇-a**, and **Pt₈-a**, the computed adsorption energies are -26.26, -31.49, -36.81, and -42.77 eV, respectively. Because of the surface reconstruction caused by Pt adsorption, the average Pt-Pt distance in **Pt₈-a** (2.64 Å) becomes shorter than that in **Pt₄-a** (2.72 Å). Interestingly, the growth energies for the second Pt chain are larger than the corresponding values for the first Pt chain, i.e., $E_{growth}(Pt_{6,ads}) > E_{growth}(Pt_{2,ads})$, $E_{growth}(Pt_{7,ads}) > E_{growth}(Pt_{3,ads})$, and $E_{growth}(Pt_{8,ads}) > E_{growth}(Pt_{4,ads})$.

In comparison, the branched structures **Pt₅-b**, **Pt₆-b**, and **Pt₇-b** in aggregated mode b are slightly preferred in energy than **Pt₅-a**, **Pt₆-a**, **Pt₇-a**, respectively (-26.40 vs. -26.26 eV, -31.84 vs. -31.49 eV, and -37.41 vs. -36.81 eV). In **Pt₅-b**, the additional Pt atom adsorbs nearby the Pt chain and coordinates with two Fe#1 and two Pt atoms. Based on **Pt₅-b**, **Pt₆-b**, **Pt₇-b**, and **Pt₈-b** are formed by adding Pt atoms at the most stable 6F sites. **Pt₈-b** (-42.68 eV) and **Pt₈-a** (-42.77 eV) have very close adsorption energies.

Deducing from **Pt₈-a**, the most stable configurations, **Pt₉-a** and **Pt₁₀-a**, are obtained. The computed adsorption energies are also close to those deduced from **Pt₈-b** (-48.16 vs. -48.22 eV for Pt_9; -53.88 vs. -53.91 eV for Pt_{10}). After that, the aggregated modes, a and b, converge on the same most stable configuration **Pt₁₁-a** (-59.82 eV). Further addition of Pt atoms leads to the formation of the banding adsorption configuration (**Pt₁₂-a**, -66.03 eV) with three Pt chains linking together side by side.

Except for the 2D growth modes, we also consider the possibility for the 3D growth. As shown in Table 2, the adsorption energy (-19.92 eV) of a stretched tetrahedral Pt_4 cluster (**Pt₄-c**) is 1.37 eV lower than that of **Pt₄-a**. The most stable three dimensional Pt_5 cluster (**Pt₅-c**) has one stretched tetrahedral Pt_4 unit and one 6-fold Pt atom on one edge, and the adsorption energy (-25.40 eV) is 1.00 eV lower than that of **Pt₅-b**. Among twelve 3D adsorption configurations of Pt_6 clusters, the most stable one (**Pt₆-c**; -30.93 eV) by adding one Pt atom at the 6F site of **Pt₅-c** is 0.91 eV less stable than **Pt₆-b**. Among eight 3D adsorption configurations of Pt_7 clusters, the most stable one (**Pt₇-c**; -36.37 eV) by adding one Pt atom on another edge at the 6F site of **Pt₆-c** is 1.04 eV less stable than **Pt₇-b**. Clearly, Pt atoms prefer to adsorb on the surface rather than to form 3D structures in which only the first layer Pt atoms interact with the exposed surface atoms, indicating stronger Fe-Pt interaction over the Pt-Pt interaction.

On the basis of the computed adsorption and average aggregation energies, we can find that both aggregated growth modes, a and b, have almost the same energetic preferences, while the dispersed mode and the 3D mode are not competitive. Therefore at low coverage, two aggregated modes can co-exist leading to the banding structure **Pt₁₂-a**, which has the highest average adsorption energy among all Pt_n (n = 1-12) adsorbed configurations. According to these results,

Catalysis Science & Technology

ARTICLE

Table 2 Adsorption energy [E(Pt$_{n/ads}$); eV], average adsorption energy [E(Pt$_{ads/av}$); eV], average aggregation energy [E$_{agg}$(Pt$_{ads}$); eV], growth energy [E$_{growth}$(Pt$_{ads}$); eV], coordination number (CN) with surface Fe and C atoms, number of Pt-Pt bond (NB-Pt), average Pt-Pt distance (d; Å) and average Bader charge (q; e) for Pt$_n$ (n = 1-12) on the Fe$_5$C$_2$(100) surface

Pt$_n$	E(Pt$_{n/ads}$)	E(Pt$_{ads/av}$)	E$_{agg}$(Pt$_{ads}$)	E$_{growth}$(Pt$_{ads}$)	CN-Fe	CN-C	NB-Pt	d	q
Pt$_1$	-4.97	-4.97	/	/	4	2	0	/	-0.21
Aggregated mode a									
Pt$_2$-a	-10.16	-5.08	-0.11	-0.22	8	3	1	2.78	-0.24
Pt$_3$-a	-15.44	-5.15	-0.18	-0.31	12	4	2	2.76	-0.25
Pt$_4$-a	-21.29	-5.32	-0.35	-0.88	12	4	4	2.72	-0.25
Pt$_5$-a	-26.26	-5.25	-0.28	0.00	16	6	4	2.63	-0.20
Pt$_6$-a	-31.49	-5.25	-0.28	-0.26	20	7	5	2.67	-0.20
Pt$_7$-a	-36.81	-5.26	-0.29	-0.35	24	7	6	2.68	-0.21
Pt$_8$-a	-42.77	-5.35	-0.38	-0.99	24	8	8	2.64	-0.18
Pt$_9$-a	-48.16	-5.35	-0.38	-0.42	26	8	11	2.64	-0.17
Pt$_{10}$-a	-53.88	-5.39	-0.42	-0.75	28	8	15	2.66	-0.16
Pt$_{11}$-a	-59.82	-5.44	-0.47	-0.97	27	8	19	2.71	-0.14
Pt$_{12}$-a	-66.03	-5.50	-0.53	-1.24	24	8	24	2.75	-0.12
Pt$_{16}$-a	-88.40	-5.53	-0.56	/	32	4	48	2.65	-0.14
Aggregated mode b									
Pt$_5$-b	-26.40	-5.28	-0.31	-0.14	15	4	6	2.67	-0.20
Pt$_6$-b	-31.84	-5.31	-0.34	-0.47	18	6	7	2.66	-0.19
Pt$_7$-b	-37.41	-5.34	-0.37	-0.59	22	7	8	2.67	-0.18
Pt$_8$-b	-42.68	-5.34	-0.37	-0.31	25	8	10	2.68	-0.18
Pt$_9$-b	-48.22	-5.36	-0.39	-0.56	27	8	11	2.59	-0.17
Pt$_{10}$-b	-53.91	-5.39	-0.42	-0.72	30	7	15	2.68	-0.17
Dispersed mode									
Pt$_2$-d	-9.90	-4.95	0.02	0.04	8	4	0	/	-0.20
Pt$_3$-d	-14.79	-4.93	0.04	0.08	12	6	0	/	-0.18
Pt$_4$-d	-19.65	-4.91	0.06	0.11	16	8	0	/	-0.17
Three-dimensional mode									
Pt$_4$-c	-19.92	-4.98	-0.01	0.49	8	3	5	2.65	-0.21
Pt$_5$-c	-25.40	-5.08	-0.11	-0.51	12	4	6	2.65	-0.19
Pt$_6$-c	-30.93	-5.16	-0.19	-0.57	12	4	8	2.62	-0.20
Pt$_7$-c	-36.37	-5.20	-0.23	-0.46	19	6	10	2.67	-0.18

we can further deduced that as the coverage of Pt additive increases, Pt will aggregate via line-band-layer mode on Fe$_5$C$_2$(100) surface, depending on the relative intensity of Fe-Pt to Pt-Pt interactions and its surface structure. In order to verify

this conclusion we also computed the adsorption of Pt$_{16}$ clusters on Fe$_5$C$_2$(100) surface.

As shown in Fig. 4, the 2D model is a mono-layer structure (**Pt$_{16}$-a**) similar to Pt(111) surface, while the most stable 3D configuration (**ESI†** Fig. S6) has a bi-layer structure with only
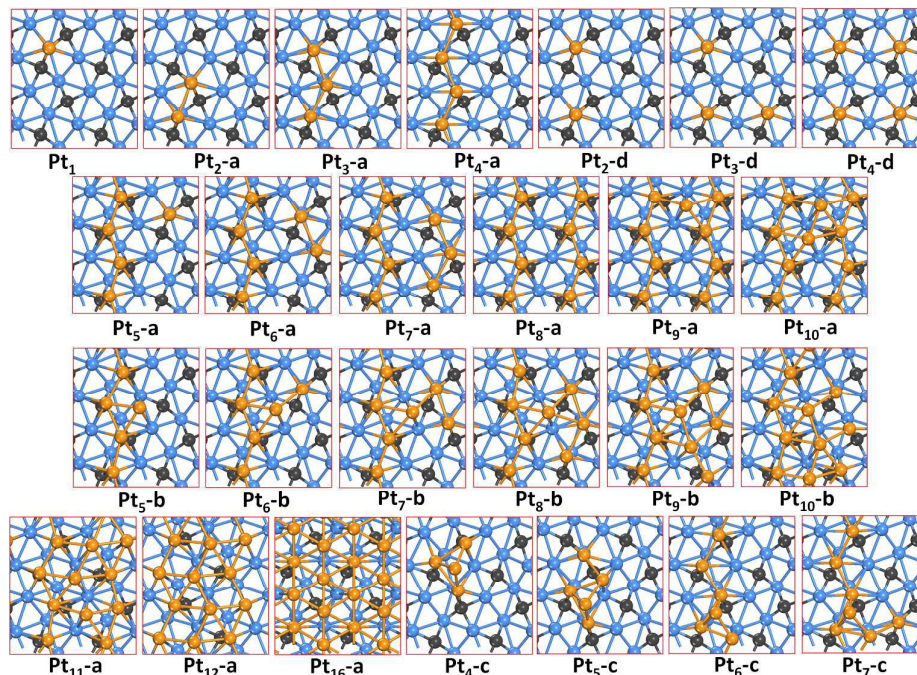
Catalysis Science & Technology

ARTICLE

Fig. 4 Structures for Pt_n (n = 1–12, 16) on the Fe_5C_2(100) surface (blue balls for Fe atoms; and orange balls for Pt atoms)

one Pt atom on the second layer. The average Pt-Pt distance of **Pt_{16}-a** is shorter than that in bulk (2.65 vs 2.77 Å) indicating a stronger interaction between Pt atoms on Fe_5C_2(100) surface. As expected, the 2D adsorption configuration (-88.40 eV) is energetically more favored than the 3D adsorption configuration (-87.21 eV), which reveals a layer-by-layer mode for further growth of Pt on Fe_5C_2(100) surface.

3.2.2. Mobility of single Pt atom. Different pathways for single Pt atom diffusion among the most stable adsorption sites (6F) on Fe_5C_2(100) surface has been examined. As shown in Fig. 5a, Pt atom may diffuse along the [001] or [010] directions resulting in the formation of Pt chains. Diffusion along the [010] direction (**Px**: **6F → TS1 → 6F**) occurs easily with a low energy barrier of 0.43 eV, while migration along the [001] direction (**Py**: **6F → 3F → 2F → 6F**) can proceed by climbing 1.01 eV in energy and no transition states could be located between **6F** and **2F** owing to the flat potential energy surface near 2F, that is, the potential energy is unidirectionally increasing from 6F to 2F.

To further study the effects of nearby Pt atom to Pt migration, Pt atom (Pt_a and Pt_b) diffusion along the [001] direction on the Pt pre-adsorbed Fe_5C_2(100) surface was also

considered, and the possible pathways (**Py1** and **Py2**) are shown in Fig. 5b. It is noted that on the **2F1** and **2F2** sites, Pt
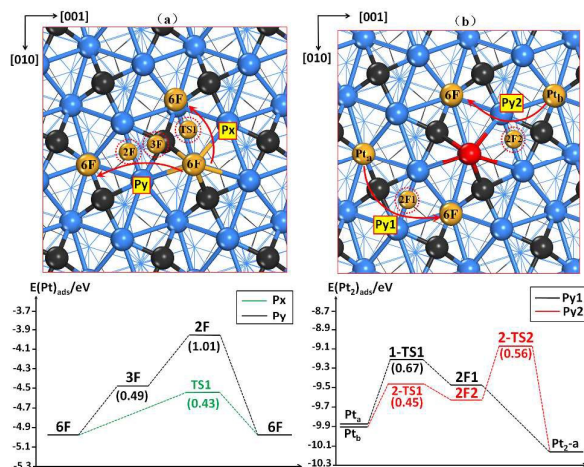

Fig. 5 Diffusion pathways of single Pt atom on the clean (a) and Pt pre-adsorbed (b) Fe_5C_2(100) surface; Numbers in the parentheses indicate the barriers. (orange balls for mobile Pt atoms and red ball for pre-adsorbed Pt atom)

atom not only coordinates with two Fe#1 atoms but also links with the pre-adsorbed Pt atom forming aggregated Pt_2 structure. As a result, the energies of **2F1** and **2F2** (Fig. 5b) decrease largely compared to that of **2F** (Fig. 5a). For **Py1**, Pt_a migrates to **2F1** ($Pt_a \rightarrow$ **1-TS1** $\rightarrow$ **2F1**) with a moderate barrier of 0.67 eV, and further migrates to **6F** (**2F1** $\rightarrow$ **6F**) without barrier. For **Py2**, the first step ($Pt_b \rightarrow$ **2-TS1** $\rightarrow$ **2F2**) occurs easily with a lower barrier of 0.45 eV, while the subsequent migration (**2F2** $\rightarrow$ **2-TS2** $\rightarrow$ **6F**) has a barrier of 0.56 eV due to the Pt-Pt interaction in **2F2**. Both of the pathways are exothermic. It is clear that the effective barrier for Pt atom diffusion between the most stable adsorption sites along [001] direction on Pt pre-adsorbed surface is decreased by the assistance of pre-adsorbed Pt atom comparing with that on the clean surface (0.67 and 0.83 vs. 1.01 eV), resembling an autocatalytic aggregation. The results demonstrate that it is not only thermodynamically but also dynamically facile for Pt_n forming aggregated configurations rather than dispersed configurations.

3.3. Pt_n Adsorption on Fe_5C_2(111) Surface

As on the Fe_5C_2(100) surface, all the possible Pt adsorption sites are considered. The structure of Fe_5C_2(111) surface and optimized adsorption sites of single Pt atom on it are shown in Fig. 2b. Unlike Fe_5C_2(100), the Fe_5C_2(111) surface is rugged with Fe and C atoms in more disordered arrangement. So, the Fe_5C_2(111) surface has five different sites for single Pt atom adsorption, which are seven-fold site (7F), six-fold site (6F), three four-fold sites (4F1, 4F2, and 4F3). The 7F site locates in the concave position of the surface and consists of four Fe atoms and three C atoms. The 6F site consists of five Fe atoms and one C atom. All four-fold sites (4F1, 4F2, and 4F3) consist of three Fe atoms and one C atom.

For Pt_n ($n \geq 4$), three adsorption modes have been examined; i.e., the dispersed mode, the mono-layer aggregated (2D) mode and the three-dimensional cluster (3D) mode in which only the first layer Pt atoms interact with the exposed surface atoms. Because of the large numbers of adsorption configurations, we mainly discuss the most stable dispersed and 2D aggregated structures (Table 3 and Fig. 6), while the
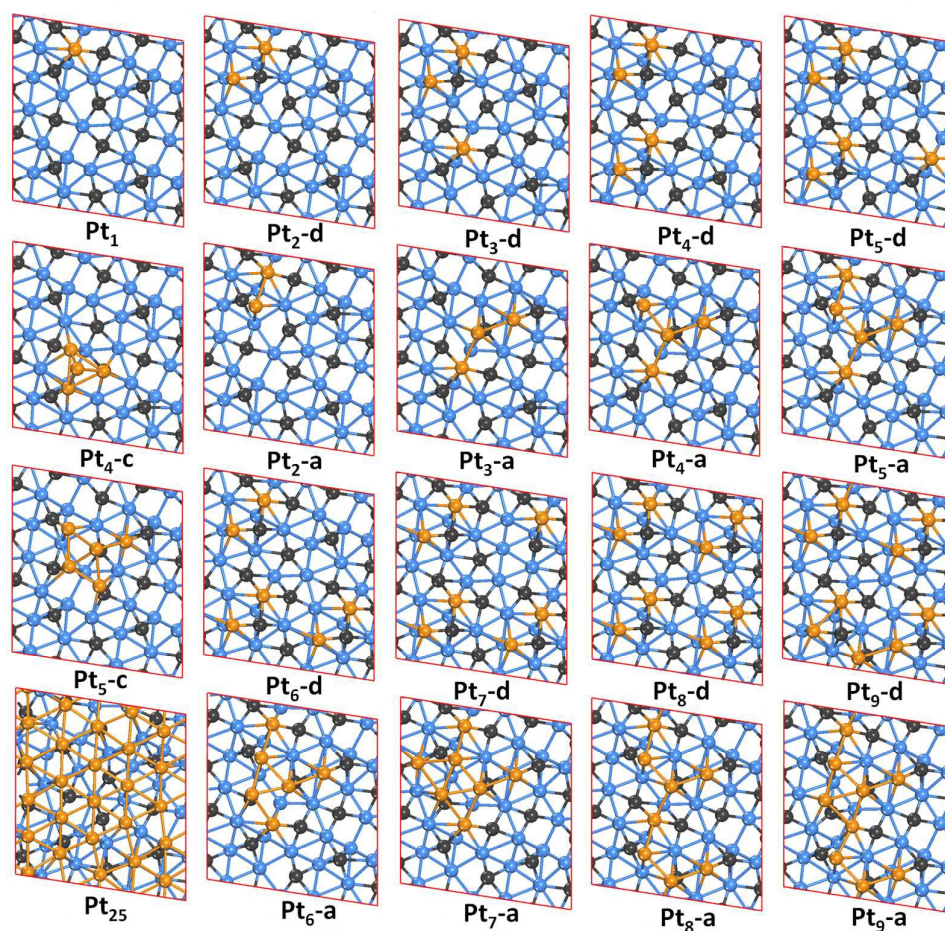
Fig. 6 Most stable adsorption configurations of Pt_n (n = 1–12) on the Fe_5C_2(111) surface (blue balls for Fe atoms, black balls for C atoms, and orange balls for Pt atoms)

other less stable adsorption structures along with their energies are given in **ESI†** for comparison. The adsorption energies of the adsorbed Pt atoms depend not only on the coordination numbers (CN) with the exposed surface iron (CN-Fe) and carbon (CN-C) atoms, but also on the specific shape of the adsorption site due to the irregularity of the surface.

3.3.1. Pt_n adsorption. The results of Pt_n (n = 1-9, 25) adsorption on the $Fe_5C_2(111)$ surface are listed in **Table 3**, and the detailed adsorption structures are shown in Fig. 6.

As shown in Fig. 6, the most stable adsorption site for single Pt atom on $Fe_5C_2(111)$ is the 7F site, and the corresponding adsorption energy is -5.59 eV. For Pt_2 adsorption, the most stable configuration is **Pt_2-d** (-11.24 eV) with two Pt atoms at the neighbor 7F and 6F sites and a elongated distance of 3.14 Å. Due to the surface reconstruction, **Pt_2-d** has a higher

average adsorption energy than **Pt_1** (-5.62 vs -5.59 eV). For the aggregated mode, **Pt_2-a** having one Pt atom at the 7F site and one Pt atom at a four-fold site is less stable.

For Pt_3 adsorption, the **Pt_3-d** is also more stable than the aggregated mode (**Pt_3-a**), and the adsorption energies are -16.88 and -16.17 eV, respectively. In **Pt_3-d**, an additional Pt atom is added to the most stable Pt_2 configuration at the 7F site, and is dispersed from the two original Pt atoms. In **Pt_3-a**, the Pt atoms are at 7F, 6F, and 4F2 sites, respectively.

For n = 4, the most stable adsorption configuration is the dispersed mode (**Pt_4-d**), which can be regarded as the combination of two **Pt_2-d**. The adsorption energy of **Pt_4-a** is -21.60 eV, which is 1.02 eV higher than that of the dispersed mode. Furthermore, the three-dimensional model (**Pt_4-c**, a tetrahedral structure) is 2.17 eV higher in energy than **Pt_4-d**.

Table 3 Adsorption energy [$E(Pt_{n/ads})$; eV], average adsorption energy [$E(Pt_{ads/av})$; eV], average aggregation energy [$E_{agg}(Pt_{ads})$; eV], growth energy [$E_{growth}(Pt_{ads})$; eV], coordination number (CN) with surface Fe and C atoms, number of Pt-Pt bond (NB-Pt), average Pt-Pt distance (d, Å), and average Bader charge (q, e) for Pt_n (n = 1-12) on the $Fe_5C_2(111)$ surface

Pt_n	$E(Pt_{n/ads})$	$E(Pt_{ads/av})$	$E_{agg}(Pt_{ads})$	$E_{growth}(Pt_{ads})$	CN-Fe	CN-C	NB-Pt	d	q
Pt_1	-5.59	-5.59	/	/	4	3	0	/	-0.01
Aggregated mode									
Pt_2-a	-10.62	-5.31	0.28	0.56	6	3	1	2.71	-0.16
Pt_3-a	-16.17	-5.39	0.20	/	13	5	2	2.73	-0.19
Pt_4-a	-21.60	-5.40	0.19	0.16	14	6	3	2.74	-0.17
Pt_5-a	-27.32	-5.46	0.13	-0.13	18	8	4	2.72	-0.15
Pt_6-a	-32.61	-5.43	0.16	0.31	20	8	6	2.72	-0.15
Pt_7-a	-38.03	-5.43	0.16	0.16	24	10	9	2.76	-0.14
Pt_8-a	-43.31	-5.41	0.18	/	26	10	8	2.69	-0.17
Pt_9-a	-48.65	-5.41	0.18	0.25	29	11	11	2.70	-0.17
Dispersed mode									
Pt_2-d	-11.24	-5.62	-0.03	-0.06	8	4	0	/	-0.12
Pt_3-d	-16.88	-5.63	-0.04	-0.05	12	7	0	/	-0.12
Pt_4-d	-22.62	-5.66	-0.07	-0.15	16	8	0	/	-0.14
Pt_5-d	-28.05	-5.61	-0.02	0.16	20	11	0	/	-0.13
Pt_6-d	-33.71	-5.62	-0.03	-0.07	27	12	0	/	-0.15
Pt_7-d	-39.18	-5.60	-0.01	0.12	31	15	0	/	-0.12
Pt_8-d	-44.99	-5.62	-0.03	-0.22	36	16	0	/	-0.15
Pt_9-d	-50.03	-5.56	0.03	0.55	36	18	3	2.86	-0.14
Three-dimensional mode									
Pt_4-c	-20.45	-5.11	0.48	/	9	3	6	2.68	-0.14
Pt_5-c	-25.78	-5.16	0.43	/	12	4	6	2.67	-0.16
Mono-layer structure									
Pt_{25}	-137.56	-5.50	0.09	/	37	12	70	2.76	-0.12

Catalysis Science & Technology

On the basis of **Pt$_4$-d**, the most stable Pt$_5$ adsorption configuration (**Pt$_5$-d**) is obtained by adding one Pt atom at the 7F site. The resulted configuration (**Pt$_5$-d**) has the larger adsorption energy than the aggregated mode **Pt$_5$-a** (-28.05 vs. -27.32 eV). For the three-dimensional model (**Pt$_5$-c**), four Pt atoms interact with the surface and one Pt atom sits at the second layer, which has the adsorption energy of -25.78 eV, and is less stable than **Pt$_5$-d** by 2.27 eV. Since 3D mode is more unstable, we only discuss the dispersed and aggregated modes for n ≥ 6.

From Fig. 6, we can see that in **Pt$_5$-d**, there still have one 7F site and two 6F sites unoccupied on the surface, so further addition of Pt atoms will take up these most stable sites in turn forming the dispersed mode. As expected, the most stable Pt$_6$, Pt$_7$ and Pt$_8$ configurations are the dispersed **Pt$_6$-d**, **Pt$_7$-d**, and **Pt$_8$-d** and the corresponding adsorption energies are -33.71, -39.18, and -44.99 eV, respectively. In comparison, the most stable aggregated structures, **Pt$_6$-a**, **Pt$_7$-a** and **Pt$_8$-a**, are 1.10, 1.15 and 1.68 eV higher in energy than the dispersed ones. The **Pt$_8$-d** configuration has four most stable Pt$_2$ units (Pt$_2$-d). Due to having the similar structure units, the **Pt$_n$** (n = 1-8) configurations of the dispersed mode have very close average adsorption energies (about -5.60 eV).

In **Pt$_8$-d**, all 7F and 6F sites have been occupied, consequently, additional Pt atoms will adsorb at the low coordinated sites. For Pt$_9$ adsorption, no totally dispersed mode can be found due to the finiteness of the surface area. The most stable configuration is the dispersed/aggregated **Pt$_9$-d** with a Pt atom added to the 4F2 site of **Pt$_8$-d**, which has a distance of 2.85 Å to the 6F site Pt atom. The most stable aggregated structure (**Pt$_9$-a**) is also less stable than **Pt$_9$-d** (-48.65 vs -50.03 eV). This indicates that, at the lower coverage (Pt/Fe ≤ 2/7, surface atom ratio), Pt prefers to adsorb in the dispersed mode on Fe$_5$C$_2$ (111). As the Pt coverage increases to Pt/Fe > 2/7, the planar aggregation will take place in local area. Actually, when the coverage of Pt atom achieves to about 0.9 ML, the mono-layer structure is formed as **Pt$_{25}$-a**, resembling the Pt (111) surface.

3.3.2. Mobility of single Pt atom. It is noted that the adsorption energies of Pt atom at the 6F (-5.08 eV) and 7F (-5.59 eV) sites are higher than the 4F sites (-4.78, -4.56, and -4.41 eV for 4F1, 4F2, and 4F3, respectively). Consequently, the Pt atoms have thermodynamic preference to adsorb at the 6F and 7F sites and form the dispersed configuration. To further understand the kinetic possibility for forming the dispersed Pt$_n$
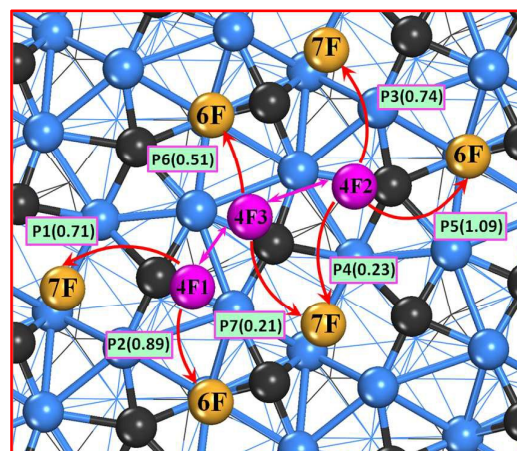
Fig. 7 Diffusion pathways and the corresponding barriers (eV) of single Pt atom on the Fe$_5$C$_2$(111) surface (purple balls for low coordinated Pt atoms and orange balls for high coordinated Pt atoms)

(n ≤ 8) on Fe$_5$C$_2$ (111), single Pt atom diffuses from the 4F1/4F2/4F3 sites to the 6F/7F sites have been examined.

As shown in Fig. 7, **P1** and **P2** are the diffusion pathways from the 4F1 sites to the 7F and 6F sites; the computed diffusion barriers are 0.71 and 0.89 eV, respectively. The diffusion barriers from the 4F2 site to two neighbor 7F sites are 0.74 eV (**P3**) and 0.23 eV (**P4**), while the barrier of the pathway **P5** is 1.09 eV. For Pt atom on 4F3 site, a 0.51 eV barrier should be overcome to migrate to the 6F site (**P6**), and the diffusion barrier to the 7F site is only 0.21 eV. All these diffusion steps are exothermic and have low or moderate barriers, indicating the facile migration for Pt atom from the less stable sites (4F1, 4F2, and 4F3) to the most stable sites (6F and 7F) on Fe$_5$C$_2$ (111) surface. It is noted that the reverse diffusions from 6F/7F sites to 4F1/4F2/4F3 is impossible to occur due to the larger endothermic property. Therefore, Pt$_n$ (n ≤ 8) tends to form the dispersed configurations on Fe$_5$C$_2$ (111) because of the thermodynamic stability as well as the dynamic feasibility.

4. discussion

It has been found that the addition of Pt promoters can improve greatly the reduction Fe oxide precursors in Fe catalysts for FTS and shift the selectivity to heavier products, and this promoting effect is related to the geometrical and electronic features of Pt on the catalyst surface. Therefore,

understanding the states of platinum on different Fe_5C_2 surfaces is very essential to R&D the Pt/Fe catalysts.

Comparing the energy data in Table 1, 2, and 3, we can find that the growth energies of Pt_n on the $Fe_5C_2(100)$ and $Fe_5C_2(111)$ surfaces are considerably lower than those in gas phase, indicating that the potential of Pt_n growth to large size on the $Fe_5C_2(100)$ and $Fe_5C_2(111)$ surfaces is lower than that in gas phase, and the stability of Pt_n on both surfaces may correlate with their surface structure. From thermodynamic point of view, the growth mode can be reflected by the trends of the average adsorption energy and the growth energy. On the $Fe_5C_2(100)$ surface, the average adsorption energy increases (become more negative) with the aggregated Pt atom number, indicating that the larger Pt_n is more stable. On the other hand, the growth energies of the aggregated mode a and b are negative and comparable, which suggests that Pt_n has stronger ability to get one more Pt atom from the surface to form the Pt_{n+1}, and both modes could co-exist. The Pt_n growth follows the line-band-layer mode forming the aggregated 2D structures rather than 3D clusters up to mono-layer on the $Fe_5C_2(100)$ surface.

In comparison, the adsorption energy of Pt atom on the $Fe_5C_2(111)$ surface is stronger than that on the $Fe_5C_2(100)$ surface, revealing a stronger surface affinity of Pt on the $Fe_5C_2(111)$ surface. This is partially because the (111) surface has a slightly more open surface structure than (100), considering that the average coordination number of surface Fe on the (111) surface is 10.86, and 11.00 on the (100) surface. Also, the (111) surface is less stable than the (100) surface according to the calculated surface energy (2.01 vs 1.82 J/m^2).[64] On $Fe_5C_2(111)$, the dispersed structures have the largest average adsorption energies. The adsorbed Pt atoms prefer to disperse on the high coordinated sites (7F and 6F) at low coverage (Pt/Fe ≤ 2/7), and began aggregation when there is no sufficient site for Pt atoms to be adsorbed separately. The positive growth energies of aggregated three dimensional modes also show that the dispersed structure is thermodynamically more favorable. On both surfaces, the 2D structures are more favorable than the 3D structures due to the strong interaction between Pt and the surface as well as the rugged surface morphology of $Fe_5C_2(111)$. Note that the adsorption energy per Pt atom for Pt monolayer is –5.53 eV on (100) and -5.50 eV on (111), which are in the same order with the calculated Pt bulk cohesive energy (-5.58 eV). The actual adsorption modes will be remarkably impacted by the experiment conditions such as the Pt concentration, temperature, acidity of the impregnation solution, etc.

Furthermore, the diffusion barriers of single Pt atom on the $Fe_5C_2(100)$ surface are moderate and can be lower by the assistance of pre-adsorbed Pt atom, indicating that the higher aggregation potential of the adsorbed Pt atoms on the $Fe_5C_2(100)$ surface kinetically. On the $Fe_5C_2(111)$ surface, Pt atom diffuses form 4F1/4F2/4F3 to 6F/7F are exothermic and have low or moderate barriers, while the reverse diffusions
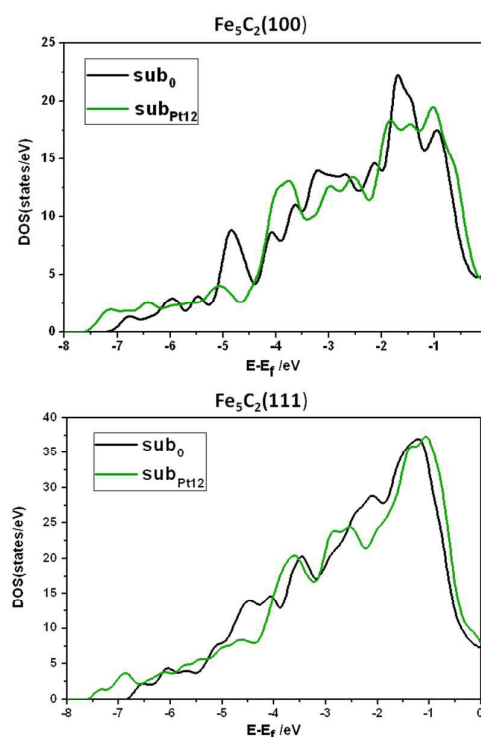
Fig. 8 DOS projected onto d orbitals （surface Fe atoms）of the Fe_5C_2 (100) and (111) surfaces before and after adsorption of Pt atoms. The Fermi levels of each system are aligned and set to 0 eV.

cannot occur thermodynamically. Therefore, Pt_n tends to form the dispersed configurations on Fe_5C_2 (111) when the surface atom ratio of Pt/Fe ≤ 2/7.

Bader charge analysis shows that the adsorbed Pt atoms on both $Fe_5C_2(100)$ and $Fe_5C_2(111)$ surfaces are negatively charged, indicating that the electrons transfer from iron carbide surface to the adsorbed Pt atoms. The density of states (DOS) of the surface Fe d orbitals of Fe_5C_2 (100) and (111) surfaces are plotted in Fig. 8. In both cases, the plots are shifted to high energy state after the Pt atoms adsorption, which also indicates the electron donation of the Fe_5C_2 surfaces. On both surfaces, the coordination numbers of Pt_n with surface C (CN-C) are less than the surface Fe (CN-Fe) atoms. The net electron transfer comes from the difference in electronegativity between Fe and Pt (1.80 for Fe; and 2.28 for Pt), although the C atom has a strong electronegativity of 2.55. Though it is demonstrated that the noble metal Pt has the opposite electronic effects compared with potassium, the Pt promoter can increase the conversion of CO and enhance the selectivity of heavy hydrocarbons.[25, 27] The mechanisms of the promotion of platinum on the iron-based catalysts deserve further study.

It is learned from a recent research that, on $Fe_5C_2(100)_{0.25}$ surface, the presence of CO stabilizes atomic copper and impedes the mobility of Cu slightly.[73] In comparison, Pt shows

**Table 4** Comparison of adsorption energy of Pt, Cu, and CO on $Fe_5C_2(100)$ and (111) surfaces.

E_{ads}		$Fe_5C_2(100)$	$Fe_5C_2(111)$
	Pt	-4.97	-5.59
	Cu^{74}	-2.84	-3.23
CO	Fe-site	-1.60	-1.58
	Pt-site	-1.72	-1.70

much stronger affinity on Fe_5C_2 surfaces than Cu,[74] indicating there are stronger interaction between Pt and support (see Table 4). The computed adsorption energy of CO on Pt/Fe_5C_2(100) is -1.72 eV, and -1.70 eV for Pt/Fe_5C_2(111) which are much lower than the adsorption energy of Pt on corresponding surfaces (-4.97 eV for (100); -5.59 eV for (111)). We propose that the strong interaction between Pt and Fe_5C_2 might inhibit the morphology changes of Pt nanoparticles. However, in Fischer-Tropsch condition, the effect of CO/H_2 ratio (or pressure) and temperature might alter the situation, and Pt might sintering somehow. The related studies are performing in our group, and will be published somewhere. In return, the charge transfer and the redistribution of electrons will have a remarkable influence on adsorption and reactions of the involved molecules.[75,76] The effects of Pt metal on the elementary reactions of FTS will be explored in our subsequent work.

The FTS reaction on iron-based catalysts often proceeds at 520~550K and the catalysts are usually calcined at the temperature over 700K.[16-20] To take the effect of temperature on the Pt_n growth modes into account, we have carried out the ab initio molecular dynamics (AIMD) calculations using a CP2K package with PBE functional. During the AIMD simulations, Fe_5C_2 (100)-p(2 × 3) and Fe_5C_2 (111)-p(2 × 2) slab models were used to model the Fe_5C_2 substrate. The thickness, fixed, and relaxed layers of the slabs are the same with those described in section 2.2. The most stable bi-layer Pt_{12} cluster in gas phase was chosen to model the initial structure of Pt cluster. The simulations were performed With the Pt_{12} cluster initially deposited at the given position as well as the annealing rump disregarded.

On both surfaces, the AIMD results show that the initial 3D structures collapsed as 2D configurations (Fig. 9) after 20 ps in the dynamics calculations in the thermostat at 1000 K, indicating the binding strengths between Pt and the substrates over the interaction between the Pt atoms, which is consistent with the conclusions from the DFT calculations. The trajectories of Pt_{12} structure evolution on the (100) and (111) surfaces from AIMD calculation are shown in **Video-S1** and **Video-S2**.† It is noted that the AIMD transformation process of Pt_{12} on the Fe_5C_2(100) surface also shows the line-band-layer growth mode. The final structure from the AIMD calculation of Pt_{12} on the Fe_5C_2(100) surface is totally the same with the lowest-energy Pt_{12} configuration obtained by DFT calculation. On the Fe_5C_2(111) surface, several Pt atoms are driven apart
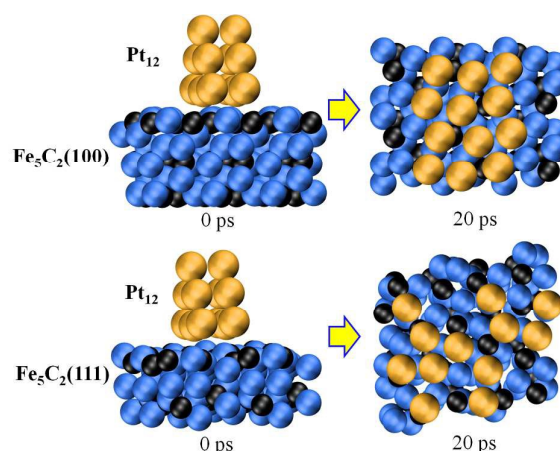
Fig. 9 The snapshot of initial and final structures at 20ps in AIMD calculation of Pt_{12} cluster deposited on the Fe_5C_2(100) and (111) surfaces. The Pt atoms are in orange, the Fe atoms in blue and the C atoms in black.

from the initial Pt_{12} cluster by the strong affinity from the substrate. The final structure is partially dispersed with almost all the most stable sites (6F and 7F) occupied, which is similar to the lowest-energy Pt_{12} configuration from DFT calculation. As seen from the result, the equilibrium structures after 20 ps are totally distorted by the strong interaction with the corresponding surfaces and in consistent with the growth moods obtained from the DFT calculations. The final structures show little resemblance with the initial ones, which is also demonstrated by the similar calculations with different initial structures (show in †Fig. S13 and S14). Therefore, under the realistic iron-based FT reaction conditions, the Pt promoter tends to aggregate on the Fe_5C_2(100) surface following the line-band-layer mode, while prefers to disperse on the Fe_5C_2(111) surface. Such changes of Pt morphology with tuned electronic structure spontaneously cause the shifting the selectivity of F-T products.

5. Conclusions

The adsorption structures and energies of the Pt_n (n = 1-12) clusters on the Fe_5C_2(100) and Fe_5C_2(111) surfaces have been systemically predicted by using spin-polarized density functional theory method, and the morphology of Pt promoter on Hägg carbide under the realistic iron-based FT reaction conditions is determined based on the AIMD calculations. It is found that the morphology of Pt promoter on Hägg carbide highly relies on its surface structure.

On the Fe_5C_2(100) surface, the adsorbed Pt atoms favor aggregation instead of dispersion, and the aggregation takes place very easily due to the moderate diffusion barrier as well as the negative aggregation and growth energies. Furthermore, the adsorbed Pt atoms prefer to firstly aggregating as lines and grow up to band structures.

On the Fe$_5$C$_2$(111) surface with rugged surface morphology, the adsorbed Pt atoms prefer to disperse separately on the most stable sites due to the thermodynamic preference of the sites and the high barriers for the trapped Pt atoms to escape from the sites.

Monolayer adsorption configurations on both surfaces are more favorable thermodynamically than the two-layer adsorbed structures because of the stronger Fe-Pt interaction over the Pt-Pt bonding. It is therefore to expect that the adsorbed Pt atoms almost grow on surfaces as a layer by layer mode at the initial stage.

For comparison, Pt$_n$ adsorbs more strongly on the Fe$_5$C$_2$(111) surface than that on the Fe$_5$C$_2$(100) surface due to the more open structure of the (111) surface with more unsaturated Fe atoms, indicating the different Pt$_n$ morphologies on various surfaces of Hägg carbide. Stronger charge transfer from surface to the adsorbed Pt$_n$ has been found on the latter than on the former, especially at low coverage. We propose that the morphology of Pt nanoparticles can be tuned by Fe$_5$C$_2$ surfaces; to put it another way, the morphology of Pt nanoparticles will be tuned with the changes of Fe$_5$C$_2$ morphology during the reaction.

Acknowledgements

Notes and references

(1) F. Fischer and H. Tropsch, *Brennstoff Chem.,* 1923, **4**, 276–285.
(2) F. Fischer and H. Tropsch, *Brennstoff Chem.,* 1926, **7**, 97–116.
(3) K. Jothimurugesan, J. G. Goodwin, J. S. K. Gangwal and J. J. Spivey, *Catal. Today,* 2000, **58**, 335–344.
(4) Y. Jin and A. K. Datye, *J. Catal.,* 2000, **196**, 8–17.
(5) M. D. Shroff, D. S. Kalakkad, K. E. Coulter, S. D. Köhler, M. S. Harrington, N. B. Jackson, A. G. Sault and A. K. Katye, *J. Catal.,* 1995, **156**, 185–207.
(6) J. W. Niemantsverdriet, A. M. Van der Kraan, W. L. Van Dijk and H. S. Van der Baan, *J. Phys. Chem.,* 1980, **84**, 3363–3370.
(7) A. K. Datye, Y. M. Jin, L. Mansker, R. T. Motjope, T. H. Dlamini and N. J. Coville, *Stud. Surf. Sci. and Catal.,* 2000, **130**, 1139–1144.
(8) K. R. P. M. Rao, F. E. Huggins, V. Mahajan, G. P. Huffman, D. B. Bukur, and V. U. S. Rao, *Hyperfine Interact,* 1994, **93**, 1751–1754.
(9) T. Herranz, S. Rojas, F. J. Pérez-Alonso, M. Ojeda, P. Terreros and J. L. G. Fierro, *J. Catal.,* 2006, **243**, 199–211.
(10) E. Smit, A. M. Beale, S. Nikitenko and B. M. Weckhuysen, *J. Catal.,* 2009, **262**, 244–256.
(11) C. Yang, H. Zhao, Y. Hou and D. Ma, *J. Am. Chem. Soc.,* 2012, **134**, 15814–15821.
(12) T. S. Rahman, S. Stolbov and F. Mehmood, *Appl. Phys. A,* 2007, **87**, 367–374.
(13) Z. P. Liu and P. Hu, *J. Am. Chem. Soc.,* 2001, **123**, 12596–12604.
(14) M. H. Mahyuddin, R. V. Belosludov, M. Khazaei, H. Mizuseki and Y. Kawazoe, *J. Phys. Chem. C,* 2011, **115**, 23893–23901.
(15) J. Gaube and H. F. Klein, *Appl. Catal. A: Gen.,* 2008, **350**, 126–132.
(16) W. Ngantsoue-Hoc, Y. Zhang, R. J. O'Brien, M. Luo and B. H. Davis, *Appl. Catal. A: Gen.,* 2002, **236**, 77–89.
(17) H. Wan, B. Wu, T. Li, Z. Tao, X. An, H. W. Xiang and Y. W. Li, *J. Fuel Chem. Technol.,* 2007, **35**, 589–594.
(18) H. Suo, S. Wang, C. Zhang, J. Xu, B. Wu, Y. Yang, H. W. Xiang and Y. W. Li, *J. Catal.,* 2012, **286**, 111–123.
(19) Z. H. Chonco, L. Lodya, M. Claeys and E. Steen, *J. Catal.,* 2013, **308**, 363–373.
(20) C. H. Zhang, Y. Yang, B. T. Teng, T. Z. Li, H. Y. Zheng, H. W. Xiang and Y. W. Li, *J. Catal.,* 2006, **237**, 405–415.
(21) W. Ma, G. Jacobs, R. A. Keogh, D. B. Bukur and B. H. Davis, *Appl. Catal. A: Gen.,* 2012, **437-438**, 1–9.
(22) T. Jermwongratanachai, G. Jacobs, W. Ma, W. D. Shafer, M. K. Gnanamani, P. Gao, B. Kitiyanan, B. H. Davis, J. L.S. Klettlinger, C. H. Yen, D. C. Cronauer, A. J. Kropf and C. L. Marshall, *Appl. Catal. A: Gen.,* 2013, **464-465**, 165–180.
(23) D. Xu, W. Li, H. Duan, Q. Ge and H. Xu, *Catal. Lett.,* 2005, **102**, 229–235.
(24) G. Jacobs, T. K. Das, Y. Zhang, J. Li, G. Racoillet and B. H. Davis, *Appl. Catal. A: Gen.,* 2002, **233**, 263–281.
(25) J. Xu, C. H. Bartholomew, J. Sudweeks and D. L. Eggett, *Top. Catal.,* 2003, **26**, 55–71.
(26) J. Xu and C. H. Bartholomew, *J. Phys. Chem. B,* 2005, **109**, 2392–2403.
(27) W. Yu, B. Wu, J. Xu, Z. Tao, H. W. Xiang and Y. W. Li, *Catal. Lett.,* 2008, **125**, 116–122.
(28) V. I. Kovalchuk and B. N. Kuznetsov, *J. Mol. Catal. A: Chem.,* 1995, **102**, 103–110.
(29) M. Luo, R. O'Brien and B. H. *Catal. Lett.,* **2004**, *98*, 17–22.
(30) M. Minnermann, S. Pokhrel, K. Thiel, R. Henkel, J. Birkenstock, T. Laurus, A. Zargham, J. Flege, V. Zielasek, E. Piskorska-Hommel, J. Falta, L. Mädler, and M. Bäumer, *J. Phys. Chem. C,* 2011, **115**, 1302–1310.
(31) N. Guan, *Chin. J. Catal.,* 1996, **17**, 382–386.
(32) R. L. Garten, *J. Catal.* 1974, **35**, 232–246.
(33) S. Li, S. Krishnamoorthy, A. Li, G. D. Meitzner and E. Iglesia, *J. Catal.,* 2002, **206**, 202–217.
(34) L. Wang, B. Wu and Y. W. Li, *Chin. J. Catal.,* 2011, **32**, 495–501.
(35) M. A. Vannice and R. L. Garten, *J. Mol. Catal.,* 1976, **1**, 201–222.
(36) F. Viñes, J. R. B. Gomes and F. Illas, *Chem. Soc. Rev.,* 2014, **43**, 4922–4939.

(37) A. I. Frenkel, M. W. Small, J. G. Smith, R. G. Nuzzo, K. O. Kvashnina and M. Tromp, *J. Phys. Chem. C,* 2013, **117**, 23286–23294.

(38) K. Paredis, L. K. Ono, S. Mostafa, L. Li, Z. F. Zhang, J. C. Yang, L. Barrio, A. I. Frenkel and B. R. Cuenya, *J. Am. Chem. Soc.,* 2011, **133**, 6728–6735.

(39) Z. Qiu, H. Huang, J. Du, T. Feng, W. Zhang, Y. Gan and X. Tao, *J. Phys. Chem. C,* 2013, **117**, 13770–13775.

(40) B. Qiao, A. Wang, X. Yang, L. F. Allard, Z. Jiang, Y. Cui, J. Liu, J. Li and T. Zhang, *Nat. Chem.,* 2011, **3**, 634–641.

(41) M. Moses-DeBusk, M. Yoon, L. F. Allard, D. R. Mullins, Z. Wu, X. Yang, G. Veith, G. M. Stocks and C. K. Narula, *J. Am. Chem. Soc.,* 2013, **135**, 12634–12645.

(42) G. Kresse and J. Furthmüller, *Comput. Mater. Sci.,* 1996, **6**, 15–50.

(43) G. Kresse and J. Furthmüller, *Phys. Rev. B,* 1996, **54**, 11169–11186.

(44) P. Janthon, S. M. Kozlov, F. Viñes, J. Limtrakul and F. Illas, *J. Chem. Theory Comput.* 2013, **9**, 1631–1640.

(45) C. Kunkel, F. Viñes, and F. Illas, *Energy Environ. Sci.,* 2016, **9**, 141–144.

(46) J. P. Perdew, K. Burke and M. Ernzerhof, *Phys. Rev. Lett.,* 1996, **77**, 3865–3868.

(47) J. P. Perdew and Y. Wang, *Phys. Rev. B,* 1992, **45**, 13244–13249.

(48) P. E. Blochl, *Phys. Rev. B,* 1994, **50**, 17953–17979.

(49) G. Kresse, *Phys. Rev. B,* 1999, **59**, 1758–1775.

(50) H. Jónsson, G. Mills and K.W. Jacobsen, *World Scientific, Hackensack, NJ*, 1998, 385–404.

(51) G. Henkelman, B.P. Uberuaga and H. Jónsson, *J. Chem. Phys.,* 2000, **113**, 9901–9904.

(52) G. Henkelman and H. Jónsson, *J. Chem. Phys.,* 2000, **113**, 9978–9985.

(53) http://www.cp2k.org/, 2014.

(54) J. VandeVondele, M Krack, F. Mohamed, M. Parrinello, T. Chassaing and J. Hutter, *Comput. Phys. Commun.,* 2005, **167**, 103–128.

(55) J. VandeVondele and J. Hutter, *J. Chem. Phys.,* 2007, **127**, 114105.

(56) B. G. Lippert, J. Hutter and M. Parrinello, *Mol. Phys.,* 1997, **92**, 477–488.

(57) S. Goedecker, M. Teter and J. Hutter, *Phys. Rev. B,* 1996, **54**, 1703–1710.

(58) M. Krack, *Theor. Chem. Acc.,* 2005, **114**, 145–152.

(59) S. Nosé, *J. Chem. Phys.,* 1984, **81**, 511–519.

(60) W. G. Hoover, *Phys. Rev.* A, 1985, **31**, 1695–1697.

(61) X. Tian, T. Wang, Y. Yang, Y. W. Li, J. Wang and H. Jiao, *J. Phys. Chem. C,* 2014, **118**, 21963–21974

(62) X. Li and L. Wang, *J. Phys. Chem. A,* 2004, **108**, 8605–8614.

(63) J. J. Retief, *Powder Diffr.,* 1999, **14**, 130–132.

(64) S. Zhao, X. Liu, C. Huo, Y. W. Li, J. Wang and H. Jiao, *J. Catal.,* 2014, **317**, 158–166.

(65) M. N. Huda, M. K. Niranjan, B. R. Sahu and L. Kleinman, *Phys. Rev. B,* 2006, **73**, 053201.

(66) I. Fampiou and A. Ramasubramaniam, *J. Phys. Chem. C,* 2012, **116**, 6543–6555.

(67) B. Hamad, Z. El-Bayyari and A. Marashdeh, *Chem. Phys.,* 2014, **443**, 26–32.

(68) K. Bhattacharyya and C. Majumder, *Chem. Phys. Lett.,* 2007, **446**, 374–379.

(69) A. Nie, J. Wu, C. Zhou, S. Yao, C. Luo, R. C. Forrey and H. Cheng, *Int. J. Quantum Chem.,* 2007, **107**, 219–224.

(70) A. Sebetci and Z. B. Güvenc, *Surf. Sci.,* 2003, **525**, 66–84.

(71) Y. Liu, W. Cen, G. Feng, Y. Chu, D. Kong and H. Yin, *Appl. Surf. Sci.,* 2014, **313**, 424–431.

(72) S. K. Gupta, B. M. Nappi and K. A. Gingerich, *Inorg. Chem.,* 1981, **20**, 966–969

(73) E. van Steen and M. Claeys, *Catal. Struct. React.,* 2014, **000**, 1-8.

(74) X. Tian, T. Wang, Y. Yang, Y. W. Li, J. Wang and H. Jiao, *J. Phys. Chem. C,* 2015, **119**, 7371–7385.

(75) J. A. Rodriguez, P. Liu, F. Viñes, F. Illas, Y. Takahashi and K.Nakamura, *Angew. Chem. Int. Ed.,* 2008, **47**, 6685–6689.

(76) J. A. Rodriguez, P. Liu, Y. Takahashi, K. Nakamura, F. Viñes and F. Illas, *J. Am. Chem. Soc.* 2009, **131**, 8595–8602.